

Establishing a highly closed cycling transition in a polyatomic molecule

Louis Baum,^{1,2,*} Nathaniel B. Vilas,^{1,2} Christian Hallas,^{1,2}
Benjamin L. Augenbraun,^{1,2} Shivam Raval,^{1,2} Debayan Mitra,^{1,2} and John M. Doyle^{1,2}

¹Harvard-MIT Center for Ultracold Atoms, Cambridge, MA 02138, USA

²Department of Physics, Harvard University, Cambridge, MA 02138, USA

(Dated: June 3, 2020)

We study optical cycling in the polar free radical calcium monohydroxide (CaOH) and establish an experimental path towards scattering $>10^4$ photons. We report vibrational branching ratio measurements with accuracy at the $\sim 5 \times 10^{-4}$ level and observe weak symmetry-forbidden decays to bending modes with non-zero vibrational angular momentum. Quantitative theory is developed to explain these observations and predict additional decay pathways. Additionally, we perform high-resolution spectroscopy of the $\tilde{X}^2\Sigma^+(12^0_0)$ and $\tilde{X}^2\Sigma^+(12^2_0)$ hybrid vibrational states of CaOH. These advances establish a path towards radiative slowing, 3D magneto-optical trapping, and sub-Doppler cooling of CaOH.

I. INTRODUCTION

Laser cooling, one of the cornerstones of atomic, molecular and optical physics [1, 2], has enabled wide-ranging scientific applications including ultra-precise clocks [3], quantum simulation of many body systems [4], and novel quantum computation platforms [5–7]. Extension of laser cooling techniques to polyatomic molecules is at the forefront of efforts to produce ultracold samples of polyatomic species. Ultracold polyatomic molecules have been proposed for a wide range of multidisciplinary applications, including quantum simulation [8, 9] and computation [10], quantum chemistry and collisions [11, 12], and tests of fundamental physics, including searches for the electron electric dipole moment (eEDM) [13], ultralight dark matter [14], and fundamental parity violation [15].

In the past several years, enormous strides have been made in direct laser cooling of polyatomic molecules, with molecular beams of SrOH [16, 17], YbOH [18], CaOH [19], and CaOCH₃ [20] all cooled near or below 1 mK in one transverse dimension. The ability to rapidly scatter a large number of photons is at the heart of these cooling techniques, which require an estimated 10^4 scattered photons for successful confinement in a magneto-optical trap (MOT). Thus far, experimental efforts have successfully enabled scattering up to $\sim 10^3$ photons in polyatomic molecules [18, 19].

To establish a path to a MOT, vibrational branching ratios (VBRs) need to be determined with accuracy at, or exceeding, the 10^{-4} level. Measurements of VBRs have previously been performed in polyatomic molecules using dispersed laser fluorescence [21–23]. However, previously reported measurements of CaOH using this technique [21] do not provide sufficient sensitivity to identify the loss channels needed to scatter 10^4 photons.

In this work, we describe a measurement of VBRs in CaOH by detecting accumulated population in excited vibrational levels after hundreds of photons are scattered. Photon cycling enhances the measurement sensitivity, probing VBRs at the 10^{-4} level. Several weak, symmetry-forbidden decays

are observed. We describe and benchmark calculations of VBRs that include vibronic perturbations not considered in previous work. Using these calculations, we propose a photon cycling scheme capable of scattering an average of $>10^4$ photons per molecule. Finally, we perform high-resolution spectroscopy of the $\tilde{X}^2\Sigma^+(12^0_0)$ and $\tilde{X}^2\Sigma^+(12^2_0)$ hybrid vibrational modes. It is expected that repumping one or both of these states will be necessary to enable radiative slowing, trapping, and sub-Doppler cooling of CaOH.

II. VIBRATIONAL BRANCHING OVERVIEW AND MEASUREMENTS

In order to create a sustained cycling transition in CaOH, it is necessary to close loss channels due to both vibration and rotation. The relative probability of spontaneous decay to different vibrational states is described by vibrational branching ratios (VBRs). These are closely related to the Franck-Condon factors (FCFs) of the molecule, defined by the overlap integral between vibrational wavefunctions in the ground and excited states (see section III). CaOH is an example of a broad class of polyatomic molecules that have been identified as amenable to laser cooling due to strong electronic transitions and near-diagonal FCFs [21, 24, 25].

The main laser cooling transition in CaOH is the $\tilde{X}^2\Sigma^+(000) \rightarrow \tilde{A}^2\Pi_{1/2}(000)$ transition. Vibrational states are labeled with the quantum numbers (v_1, v_2^l, v_3) , where v_1 , v_2 , and v_3 are the number of quanta in the symmetric (predominantly Ca–O) stretching, bending, and antisymmetric (predominantly O–H) stretching modes, respectively. l labels the nuclear orbital angular momentum in the bending mode [26]. The highly diagonal FCFs of the $\tilde{A}^2\Pi_{1/2}(000)$ state suppress spontaneous decay to excited vibrational states during each scattering event; nonetheless, some excited vibrational states must be repumped due to significant optical pumping after many photons are scattered. In this work, we experimentally characterize the photon cycling scheme depicted in Fig. 1 and show that it is capable of scattering >2000 photons. Note that multiple excited electronic states are used to cycle photons, which must be taken into account when comparing measured

* louisbaum@g.harvard.edu

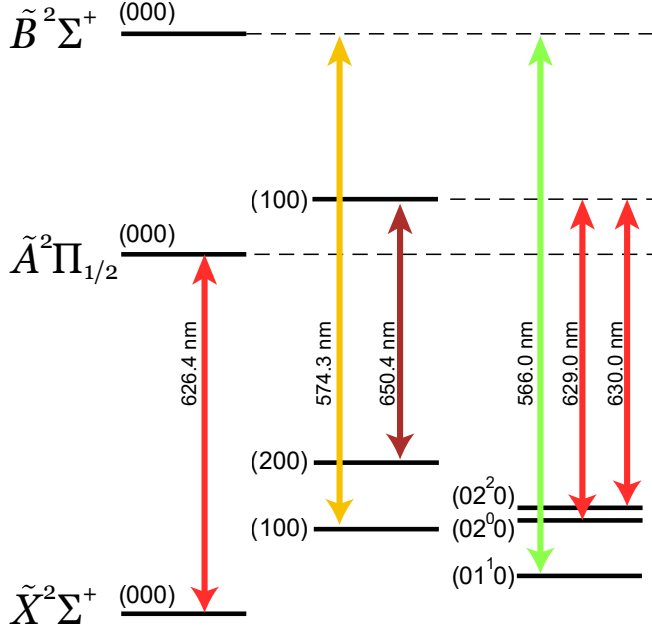


Figure 1. Photon cycling scheme and vibrational structure of CaOH considered experimentally in this work. All known vibrational states populated by decay above the 2×10^{-4} level are shown.

and calculated VBRs as discussed in section III.

For states with $l = 0$, rotational losses are prevented by driving the P_1 ($N'' = 1$) and $^P Q_{12}$ ($N'' = 1$) transitions [27]. In the ground electronic state of CaOH ($\tilde{X}^2\Sigma^+$), the $N'' = 1$ manifold is split by the spin-rotation interaction into $J'' = 1/2$ and $J'' = 3/2$ components separated by 52 MHz. Both components are addressed by using an acousto-optic modulator (AOM) to add a frequency-shifted sideband to the laser light. All hyperfine splittings are below the natural linewidth of the optical transition (Fig. 2(a)). For states with $l \neq 0$, parity doubling additionally enables decay to $N'' = 2$, which must also be addressed to achieve full rotational closure (Fig. 2(b,c)).

CaOH molecules are produced using a cryogenic buffer gas source described in previous work [19] and depicted in Fig. 3. Densities of $\sim 10^{10} \text{ cm}^{-3}$ in a single rotational state ($N'' = 1$) are routinely achieved. CaOH molecules are extracted from a two-stage buffer gas cell and form a cryogenic buffer-gas beam (CBGB) [29]. The CBGB is collimated by a 3×3 mm aperture to facilitate deflection measurements and ensure that all molecules are addressed with the applied laser light. After exiting the aperture, the collimated molecular beam enters an interaction region containing photon cycling lasers addressing the $\tilde{X}^2\Sigma^+(000) \rightarrow \tilde{A}^2\Pi_{1/2}(000)$ and $\tilde{X}^2\Sigma^+(100) \rightarrow \tilde{B}^2\Sigma^+(000)$ transitions.

We use a combination of two types of measurement to determine the VBRs of CaOH. First, we determine the combined VBR to the $\tilde{X}^2\Sigma^+(000)$ and $\tilde{X}^2\Sigma^+(100)$ vibrational states by deflecting the molecular beam using radiation pressure force from the photon cycling lasers. The measured deflection is used to determine the number of photons scattered

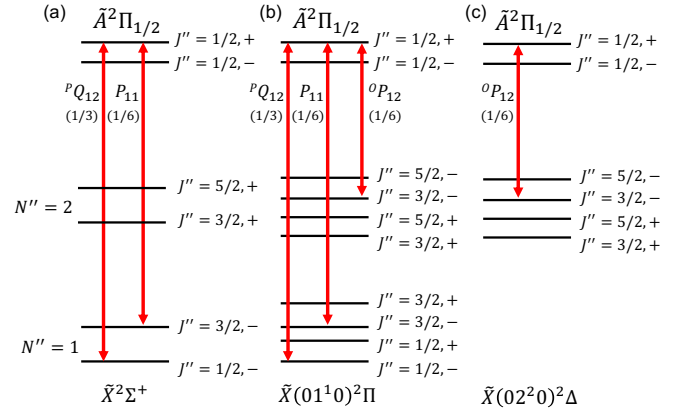


Figure 2. Allowed rotational transitions for $\tilde{X}^2\Sigma^+ \rightarrow \tilde{A}^2\Pi_{1/2}$ CaOH laser cooling. (a) All non-degenerate ground states of $^2\Sigma^+$ symmetry (e.g., (000), (100), (02⁰0)) have only two allowed rotational components split by ~ 50 MHz. Hyperfine splittings of 1.5 MHz and 7 kHz in the $J'' = \frac{3}{2}$ and $J'' = \frac{1}{2}$ states, respectively [28], are not shown. (b) Because of parity doubling in states of $^2\Pi$ symmetry (e.g., (01¹0), (11¹0)), additional decay is allowed to the $N'' = 2$ rotational level. This must be repumped using an additional laser frequency ~ 40 GHz away from the $N'' = 1$ transition. (c) States with $^2\Delta$ symmetry (e.g., (02²0), (12²0)) have no $N'' = 1$ component, so only the $^O P_{12}$ line must be addressed. Hönl-London factors for each transition are shown in parentheses.

from the deflection light. A simultaneous measurement of the molecular population depleted out of the $\tilde{X}^2\Sigma^+(000)$ and $\tilde{X}^2\Sigma^+(100)$ states during deflection allows us to extract the combined VBR, as described below. Secondly, we determine VBRs to other excited vibrational states by optically pumping molecules into these states using the same photon cycling scheme, then measuring the population increase in each state. The measurement of the accumulated population, combined with measurements of the total population lost to unaddressed levels, can be used to reconstruct the vibrational branching ratios of this laser cooling scheme.

A. Vibrational Branching Ratios to $\tilde{X}(000)$ and (100)

In the first set of measurements, the combined $\tilde{X}^2\Sigma^+(000) \rightarrow \tilde{A}^2\Pi_{1/2}(000)$ and $\tilde{X}^2\Sigma^+(100) \rightarrow \tilde{B}^2\Sigma^+(000)$ deflection lasers make a variable number of passes through the interaction region propagating in the same direction. The momentum imparted by the lasers is mapped onto a spatial deflection of the molecular beam as the molecules freely propagate to the detection region. During this propagation the $\tilde{X}^2\Sigma^+(100) \rightarrow \tilde{B}^2\Sigma^+(000)$ repumping laser is applied to recover population and ensure consistent detection efficiency. In the detection region, molecules are excited with lasers addressing the $\tilde{X}^2\Sigma^+(000) \rightarrow \tilde{B}^2\Sigma^+(000)$ and $\tilde{X}^2\Sigma^+(100) \rightarrow \tilde{B}^2\Sigma^+(000)$ transitions, and the resulting laser-induced fluorescence is imaged onto an electron mul-

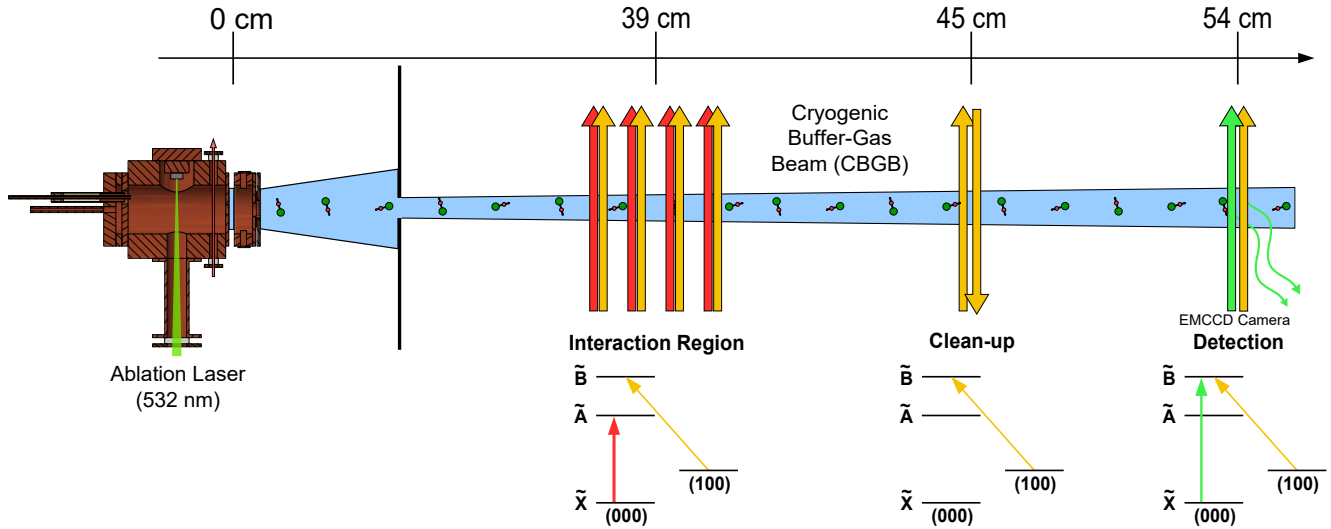


Figure 3. Experimental configuration for deflection with $\tilde{X}^2\Sigma^+(000) \rightarrow \tilde{A}^2\Pi_{1/2}(000)$ and $\tilde{X}^2\Sigma^+(100) \rightarrow \tilde{B}^2\Sigma^+(000)$ transitions. The same experimental configuration, with two modifications, is employed to measure VBRs to higher vibrational states. In this case, the laser light in the interaction region is retroreflected, and repumping lasers addressing higher vibrational levels are added in the clean-up region.

tipling charged coupled device (EMCCD) camera. The collection efficiency of the imaging system is measured to be constant over the region occupied by the molecules. The images are integrated along the direction of molecule propagation to extract spatial beam profiles, which are then fit to a Gaussian distribution. We parameterize the deflection using the center of the Gaussian fit. All data is collected with the lasers tuned to resonance.

The population remaining in detectable vibrational states after deflection can be modeled with a Bernoulli sequence as follows [27]:

$$P_f = P_i p^n \quad (1)$$

where n is the number of photons scattered, P_i is the initial molecular population, P_f is the final molecular population, and p is the total VBR back to detectable states. Note that an individual molecule scatters an average of $1/(1-p)$ photons before decaying to a dark state. To convert the magnitude of deflection into a number of scattered photons, we perform a calibration measurement by deflecting with only the main $\tilde{X}^2\Sigma^+(000) \rightarrow \tilde{A}^2\Pi_{1/2}(000)$ cycling transition. The average number of photons scattered on this transition is well known from previous measurements [21] and is scaled here to account for additional decay pathways¹. Using Eq. 1, we determine that an average of $\bar{n} = 21.7 \pm 1$ photons are scattered per molecule when only the $\tilde{X}(000)$ state is addressed. Measuring the deflection of the molecular beam in this case therefore

provides a conversion between molecular beam deflection and photon number n , which is used to determine n in subsequent measurements. We simultaneously measure the ratio of initial population to final population and extract the VBR from the following relation:

$$\log\left(\frac{P_f}{P_i}\right) = n \log(p) \quad (2)$$

Fig. 4 combines measurements where the number of photons scattered is varied by changing the deflection laser interaction length. From a fit to Eq. 2, the combined VBR to both the $\tilde{X}(000)$ and $\tilde{X}(100)$ states in this laser cooling scheme is found to be 0.9968(5).

An important systematic error in this measurement is a small Doppler shift introduced by the velocity imparted during deflection. The resulting detuning decreases the scattering rate for highly deflected molecules, reducing the apparent population in the detection region. We compensate for this effect by multiplying the observed signal by a normalization factor accounting for the difference between the effective Doppler-shifted scattering rate and the resonant scattering rate. The scattering rate is given by [30, 31]

$$R_{sc} = \frac{\Gamma_{\text{eff}}}{2} \frac{s_{\text{eff}}}{(1 + s_{\text{eff}} + 4\Delta^2/\Gamma^2)} \quad (3)$$

where Δ is the detuning of light addressing the main cycling transition, s_{eff} is the effective saturation parameter, Γ_{eff} is the effective scattering rate, and Γ is the natural linewidth. Power broadening reduces this effect.

¹ In Ref. [21] the VBRs to $\tilde{X}(000)$ and $\tilde{X}(100)$ sum to 1; however, this is unphysical given the known decay to higher vibrational states. To account for this, we scale the VBRs in Ref. [21] to the present results to determine the $\tilde{A}(000) \rightarrow \tilde{X}(000), (100)$ VBRs (e.g., $0.957 \times 0.9968 = 0.9539(21)$)

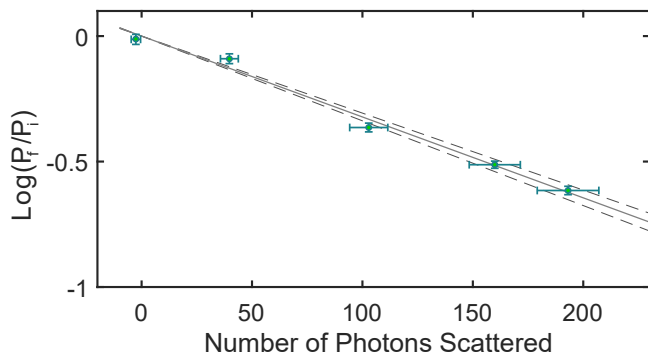


Figure 4. $\text{Log}(P_f/P_i)$ vs. number of photons scattered in deflection. The error on the x-axis is dominated by the uncertainty in \bar{n} determined for the calibration measurement, i.e., the uncertainty in the VBR from $\tilde{X}(000) \rightarrow \tilde{X}(000)$. The solid line indicates the results of a linear fit, and the dashed lines indicate the uncertainty in the fit. The results indicate that the combined VBR to both the $\tilde{X}(000)$ and $\tilde{X}(100)$ states in this laser cooling scheme is 0.9968(5).

Decay	Harmonic	Corrected ^a	Observed
(000)	0.957	0.956	0.9539(21)
(100)	0.042	0.038	0.0429(20)
(200)	0.6×10^{-3}	0.4×10^{-3}	$0.9(2) \times 10^{-3}$
(02 ⁰ 0)	1.6×10^{-4}	4.8×10^{-3}	$1.3(2) \times 10^{-3}$
(02 ² 0)	0	1.9×10^{-4}	$3.1(5) \times 10^{-4}$
(01 ¹ 0), $N'' = 1$	0	3.0×10^{-4}	$2.4(4) \times 10^{-4}$
Other	1.0×10^{-4}	2.3×10^{-4}	$4.5(7) \times 10^{-4}$

^a Corrections due to Renner-Teller and Fermi resonance couplings, as described in the text.

Table I. Comparison of calculated and observed vibrational branching ratios (VBRs) from the combined $\tilde{X}^2\Sigma^+(000) \rightarrow \tilde{A}^2\Pi_{1/2}(000) + \tilde{X}^2\Sigma^+(100) \rightarrow \tilde{B}^2\Sigma^+(000)$ photon cycling scheme used in this work. VBR calculations based on unperturbed harmonic wavefunction overlap fail to adequately capture decay to the $\tilde{X}^2\Sigma^+(02^00)$, (02^20) , and (01^10) bending modes. These discrepancies are resolved by including Fermi resonance and Renner-Teller interactions. All listed decays are to the $\tilde{X}^2\Sigma^+(v_1v_2^1v_3)$ states.

B. Vibrational Branching Ratios to $\tilde{X}(200)$, (02^00) , (02^20) , and (01^10)

In order to measure the VBRs to higher-lying vibrational states, we deplete population from the $\tilde{X}(000)$ and $\tilde{X}(100)$ states and directly measure the accumulation of molecules in excited vibrational states. In the interaction region, photon cycling lasers addressing the $\tilde{X}^2\Sigma^+(000) \rightarrow \tilde{A}^2\Pi_{1/2}(000)$ and $\tilde{X}^2\Sigma^+(100) \rightarrow \tilde{B}^2\Sigma^+(000)$ transitions are retroreflected between two mirrors for a total of ~ 12 cm of interaction distance. This interaction length is sufficient to optically pump $\sim 90\%$ of the population to higher vibrational states. We selectively recover population the states of interest by applying appropriate repumping lasers in the clean-up region.

The total loss probability must sum to 1 and the measured VBR to $\tilde{X}(000)$ and $\tilde{X}(100)$ accounts for 0.9968(5) of this total. The remaining decay probability to higher vibrational levels is assigned according to the fraction of population recovered from each state following the depletion and revival process. During these measurements we monitor both the total depletion from $\tilde{X}(000)$ and $\tilde{X}(100)$ as well as the natural population in the excited vibrational states of interest, both of which are accounted for in post-analysis. The results are summarized in Table I. The measured VBRs are in agreement with previous results [21]. While addressing the five decay pathways listed in Table I, some of the population is not recovered. We attribute this loss to yet higher-lying states and assign a corresponding VBR to all vibrational states not addressed in the laser cooling scheme in Fig. 1.

III. CALCULATED BRANCHING RATIOS

The strength of generic, dipole-allowed rovibronic decays is governed by the Einstein A coefficient [32]

$$A_{J' \rightarrow J''} = \frac{16\pi^3\nu^3 S_{J'J''}}{3\epsilon_0 hc^3 (2J' + 1)}, \quad (4)$$

where $S_{J'J''} = \sum_{M'M''} |\langle J'M'|\mu|J''M''\rangle|^2$ is the line strength of the electric dipole transition and ν is the transition frequency. This may be approximately separated into vibrational, electronic, and rotational contributions as follows:

$$S_{J'J''} \approx q_{v'-v''} |\mathbf{R}_e|^2 S_{J''}^{\Delta J'}, \quad (5)$$

where $|\mathbf{R}_e|^2$ is the electronic transition dipole moment; $S_{J''}^{\Delta J'}$ is the Hönl-London factor, which characterizes the rotational line strength (see Ref. [33] and Fig. 2); and

$$q_{v'-v''} = |\langle v''|v'\rangle|^2 \quad (6)$$

is the Franck-Condon factor (FCF). Because $|\mathbf{R}_e|^2$ is approximately constant for all transitions in an electronic band and the Hönl-London factors are known, only the FCFs must be determined in order to calculate relative line strengths, and therefore vibrational branching ratios (VBRs). Explicitly, the branching ratio from an excited state $|v'; J'\rangle$ to a ground state $|v''; J''\rangle$ is

$$P_{|v'; J'\rangle \rightarrow |v''; J''\rangle} \equiv \frac{\nu^3 q_{v'-v''} S_{J''}^{(J'-J'')}}{\mathcal{N}}, \quad (7)$$

where

$$\mathcal{N} = \sum_i \nu_i^3 q_{v'-v_i} S_{J_i}^{(J'-J_i'')} \quad (8)$$

is a normalization factor. The sum is over all ground states $|v_i''; J_i''\rangle$ to which the initial state may decay.

In section III A below, we determine FCFs for CaOH by evaluating Eq. 6 in the harmonic approximation. In sections III B and III C we consider vibronic mixing due to Renner-Teller perturbations and Fermi resonance that significantly alters the results obtained from Eqs. 4-6 alone. In section III D we combine these effects to estimate VBRs for CaOH.

A. FCF Calculations in the Harmonic Approximation

Within the harmonic approximation, Eq. 6 may be evaluated analytically using empirically measured force constants, bond lengths, and vibrational frequencies for CaOH. We evaluate these integrals by first performing a classical Wilson GF-matrix analysis of the normal modes [34], then evaluating the overlap integrals (including Duschinsky rotations) using the formalism of Sharp and Rosenstock [35, 36]. Details on this calculation are given in Appendix A. The resulting VBRs, accounting for the frequency and Hönl-London scaling factors (Eq. 7), are shown in the first column of Table I. While this calculation does a good job of reproducing observed decays to the Ca–O stretching modes, it underestimates the observed (02⁰0) bending mode decay by an order of magnitude and also fails to explain $\Delta l \neq 0$ transition strength. A more accurate description of these discrepancies requires consideration of additional perturbations.

B. Renner-Teller Perturbation

Vibrational branching to the $\tilde{X}(01^10)$ and $\tilde{X}(02^20)$ states is suppressed due to the nominal selection rule $\Delta \ell = 0$ due to the Born-Oppenheimer (BO) approximation. However, BO approximation breakdown at the level of a few parts per thousand is not unexpected. Transitions with $|\Delta \ell| = 1$ have been previously observed in SrOH [37], BaOH [38], and CaOH [39]. In this work, we consider two decays in which $|\Delta \ell| \neq 0$: $\tilde{A}^2\Pi_{1/2}(000) \rightarrow \tilde{X}^2\Sigma^+(01^10)$ and $\tilde{A}^2\Pi_{1/2}(000) \rightarrow \tilde{X}^2\Sigma^+(02^20)$. These decays are due to Renner-Teller-induced vibronic coupling. The Renner-Teller Hamiltonian has been covered in depth elsewhere [40–45].

$$\tilde{A}^2\Pi_{1/2}(000) \rightarrow \tilde{X}^2\Sigma^+(01^10) \text{ decay}$$

The $|\Delta \ell| = 1$ transition has been previously observed in several alkaline-earth monohydroxides [37–39]. This transition could gain strength due to either direct vibronic coupling between $\tilde{B}^2\Sigma^+(01^10)$ and $\tilde{A}^2\Pi_{1/2}(000)$ or through a second-order spin-orbit vibronic coupling [46]. Previous authors have favored the latter explanation based on the observation that the intensity grows with atomic spin-orbit constant [37, 39]. In this model, a unitary transformation applied to the perturbation $H_{RT} + H_{SO}$ introduces a mixing between the $\tilde{A}^2\Pi(01^10)$ and $\tilde{A}^2\Pi(000)$ states. The fraction of $|\ell| = 1$ character mixed into the nominal $|\ell| = 0$ state is [37, 47]

$$\approx \frac{2|\langle \tilde{A} | H_{RT} | \tilde{B} \rangle \langle \tilde{B} | H_{SO} | \tilde{A} \rangle|^2}{(\omega_2 E_{\tilde{A}-\tilde{B}})^2} \approx \frac{4\Delta g_L A_{SO}^2}{\omega_2^2}. \quad (9)$$

The second expression uses the pure precession and unique perturber approximations to relate each of the spin-orbit and Renner-Teller matrix elements to a measurable spectroscopic

parameter, A_{SO} and Δg_L , respectively [45]. Applying the scaling factors of Eq. 7, for the $N'' = 1$ rotational component of $\tilde{X}^2\Sigma^+(01^10)$ we arrive at a VBR of

$$P_{(000)-(01^10)} \approx \frac{v^3 q_{(01^10)-(01^10)} (S_{3/2}^P + S_{1/2}^Q)}{\mathcal{N}} \frac{4\Delta g_L A_{SO}^2}{\omega_2^2} \approx 1.9 \times 10^{-4}. \quad (10)$$

Branching to $N'' = 2$ is not included here, but is expected to become significant at the $\sim 0.5 \times 10^{-4}$ level. Additionally, vibrational branching from $\tilde{B}^2\Sigma^+(000) \rightarrow \tilde{X}^2\Sigma^+(01^10)$ contributes significantly to the observed decay, as discussed below (section III D).

$$\tilde{A}^2\Pi_{1/2}(000) \rightarrow \tilde{X}^2\Sigma^+(02^20) \text{ decay}$$

The $|\Delta \ell| = 2$ transition gains transition strength due to mixing of the $\tilde{A}^2\Pi_{1/2}(000)$ state with the $\tilde{A}^2\Pi_{1/2}(02^20)$ state by the Renner-Teller Hamiltonian. The quadrupolar term in H_{RT} can couple states according to the selection rules $\Delta \Lambda = \pm 2$, $\Delta \ell = \mp 2$, $\Delta \Sigma = 0$, and can therefore mix certain components of $\tilde{A}^2\Pi(000)$ and $\tilde{A}^2\Pi(020)$. A very similar interaction has previously been observed between $\tilde{A}^2\Pi_{1/2}(01^10)$ and $\tilde{A}^2\Pi_{1/2}(03^30)$ in CaOH [48].

The structure and labeling convention of the $\tilde{A}^2\Pi(020)$ level is discussed in detail in Refs. [49–51]. The spin-orbit and vibronic interactions split the $\tilde{A}^2\Pi(020)$ level into six components, as illustrated in figure 1 of Ref. [51]. We primarily consider the $\tilde{A}(020)\kappa^2\Pi_{1/2}$ component which, at low J' , has predominantly $|\ell| = 2$ character. H_{RT} therefore couples $\tilde{A}(020)\kappa^2\Pi_{1/2}$ and $\tilde{A}(000)^2\Pi_{1/2}$. The matrix element connecting these states is $\epsilon\omega_2/\sqrt{2}$ [48, 51]. This coupling mixes in some (02²0) character to the $\tilde{A}(000)^2\Pi_{1/2}$ level with an amplitude

$$\approx \frac{\langle \tilde{A}(020)\kappa^2\Pi_{1/2} | H_{RT} | \tilde{A}(000)^2\Pi_{1/2} \rangle}{\Delta E} \approx \frac{\epsilon\omega_2/\sqrt{2}}{\Delta E}, \quad (11)$$

where ΔE is the energy splitting between the $\tilde{A}(020)\kappa^2\Pi_{1/2}$ and $\tilde{A}(000)^2\Pi_{1/2}$ levels.

While $\epsilon\omega_2 \approx -36.26 \text{ cm}^{-1}$ has previously been measured [48], this parameter receives significant contributions from the two leading orders of the Renner-Teller Hamiltonian, $\epsilon\omega_2 = \epsilon^{(1)}\omega_2 + \epsilon^{(2)}\omega_2$. The first order term ($\epsilon^{(1)}\omega_2$) contributes to mixing between $\tilde{A}(020)\kappa^2\Pi_{1/2}$ and $\tilde{A}(000)^2\Pi_{1/2}$ (due to the V_{22} term in the notation of Ref. [45]). To remove the effects of these second-order contributions, we note that [45]

$$\epsilon^{(2)}\omega_2 \approx -\frac{2g_K \Delta E_{\tilde{B}-\tilde{A}}}{\omega_2} \quad (12)$$

$$\approx -6 \text{ cm}^{-1}, \quad (13)$$

where we have substituted the measured values from Ref. [48]. This isolates the first-order contribution to the Renner-Teller matrix element, $\varepsilon^{(1)}\omega_2 \approx -30 \text{ cm}^{-1}$. Using the measured energy splitting $\Delta E = 819 \text{ cm}^{-1}$ [51], this gives an estimated VBR of

$$P_{(000)-(02^0)} \approx \frac{v^3 q_{(02^0)-(02^0)} S_{3/2}^P}{\mathcal{N}} \left(\frac{-30 \text{ cm}^{-1}}{\sqrt{2} \times 819 \text{ cm}^{-1}} \right)^2 \approx 1.9 \times 10^{-4}. \quad (14)$$

Note that decay to $\tilde{X}(02^0)$ is suppressed in part due to the fact that only the ${}^oP_{12}$ branch is allowed in this case, while all other transitions have both ${}^pQ_{12}$ and ${}^pP_{11}$ branches (Fig. 2). This VBR is in good agreement with the measured value of $3.1(5) \times 10^{-4}$.

C. Fermi Resonance

Because the Ca–O stretching frequency is approximately double that of the Ca–O–H bending frequency in CaOH [51], vibrational states differing by $\Delta v_1 = \pm 1$, $\Delta v_2 = \mp 2$ come in closely spaced groups, e.g., $(100) \sim (020)$ and $(200) \sim (120) \sim (040)$. States of the same vibronic symmetry within these polyads are mixed by a cubic term in the potential energy surface of the form $V_F = k_{122} Q_1 Q_2^2$, where Q_1 and Q_2 are normal coordinates associated with Ca–O stretching and Ca–O–H bending, respectively. This leads to intensity borrowing which can significantly affect the magnitude of vibronic decay channels including $\tilde{X}^2\Sigma^+(02^0)$ and $\tilde{X}^2\Sigma^+(12^0)$. This effect is well understood, and is known as the Fermi resonance interaction [52, 53].

The Fermi resonance interaction is quantified by a parameter W , which is estimated to be $\approx -10.7 \text{ cm}^{-1}$ in the $\tilde{X}^2\Sigma^+$ state based on prior measurements in CaOH [51] (see Appendix B for details). Including this off-diagonal coupling within the $\tilde{X}(100) \sim (02^0)$ Fermi dyad leads to the following mixing amplitudes²:

$$\begin{aligned} |\tilde{X}(100)\rangle &= 0.96|\tilde{X}(\overline{100})\rangle + 0.28|\tilde{X}(\overline{02^0})\rangle \\ |\tilde{X}(02^0)\rangle &= -0.28|\tilde{X}(\overline{100})\rangle + 0.96|\tilde{X}(\overline{02^0})\rangle. \end{aligned} \quad (15)$$

The VBR from $\tilde{A}^2\Pi_{1/2}(000) \rightarrow \tilde{X}^2\Sigma^+(02^0)$ is then given by

$$\begin{aligned} P_{(000)-(02^0)} &\approx |0.96\langle\tilde{X}(\overline{02^0})|\tilde{A}(\overline{000})\rangle - 0.28\langle\tilde{X}(\overline{100})|\tilde{A}(\overline{000})\rangle|^2 \\ &\times \frac{v^3(S_{3/2}^P + S_{1/2}^Q)}{\mathcal{N}} \approx 4.8 \times 10^{-3}, \end{aligned} \quad (16)$$

where each inner product on the right-hand side is a harmonic overlap integral that can be evaluated using the methods of

section III A. A similar expression applies to the $\tilde{X}^2\Sigma^+(100)$ branching ratio. The Fermi resonance mixing therefore increases the branching ratio to $\tilde{X}(02^0)$ by an order of magnitude compared to the purely harmonic result.

Fermi mixing between $\tilde{X}(200)$ and $\tilde{X}(12^0)$ is also expected to cause significant branching to the $\tilde{X}^2\Sigma^+(12^0)$ state. This is predicted to be one of the primary loss channels from the photon cycling scheme in Fig. 1.

D. Calculation Results

Table I compares calculated VBRs with the experimental results of section II. The calculations generally exhibit good agreement with measured branching ratios. While branching to the Ca–O stretching modes (000) , (100) , and (200) is dominated by harmonic wavefunction overlap, decay to the bending modes arises predominantly from other mechanisms. Branching to $\tilde{X}^2\Sigma^+(02^0)$ occurs primarily due to Fermi resonance mixing with the $\tilde{X}^2\Sigma^+(100)$ state, while decay to the $l \neq 0$ bending modes (02^0) and (01^0) arises from Renner-Teller and/or spin-orbit mixing in the \tilde{A} and \tilde{B} states, as described in section III B.

For most states the $\tilde{A} \rightarrow \tilde{X}$ VBR is a good approximation to the observed branching out of the experimental cycling scheme, which employs both $\tilde{X}^2\Sigma^+(000) \rightarrow \tilde{A}^2\Pi_{1/2}(000)$ and $\tilde{X}^2\Sigma^+(100) \rightarrow \tilde{B}^2\Sigma^+(000)$ transitions. However, this is not true for the $\tilde{X}(01^0)$ state, which experiences significant decay from $\tilde{B}(000)$ with an experimentally measured VBR of $3(1) \times 10^{-3}$ [21]. To account for this, we scale the separately-determined $\tilde{A} \rightarrow \tilde{X}$ and $\tilde{B} \rightarrow \tilde{X}$ VBRs by the relative number of photon scattering events through each excited state. The effective branching ratio out of the experimental cycling scheme is therefore approximately

$$\approx 0.96\text{VBR}(\tilde{A} \rightarrow \tilde{X}) + 0.04\text{VBR}(\tilde{B} \rightarrow \tilde{X}) \quad (17)$$

since on average $\sim 96\%$ ($\sim 4\%$) of the surviving molecular population is excited from $\tilde{X}(000)$ ($\tilde{X}(100)$) based on the measured branching ratios. This correction is significant only for the $\tilde{X}(01^0)$ state, and is neglected for all other VBRs in Table I.

The final row of Table I compares the calculated and measured total branching ratio to states not addressed by the photon cycling scheme of Fig. 1. We may use the calculations to make qualitative predictions about the states that must be addressed to cycle $> 10^4$ photons in CaOH. The calculated loss is dominated by decay to $\tilde{X}^2\Sigma^+(12^0)$ at the $\sim 1 \times 10^{-4}$ level due to Fermi resonance mixing with $\tilde{X}(200)$; and by loss to the $N'' = 2$ component of $\tilde{X}(01^0)$ at the $\sim 0.5 \times 10^{-4}$ level. In anticipation of the need to repump these states, high resolution spectroscopy of the (120) manifold was performed (see Appendix C).

Additional loss channels may be more significant than these calculations indicate, gaining strength through perturbations neglected in the analysis. Specifically, though decay to

² A bar is used to denote bare harmonic oscillator eigenstates, which (in this case) are not exact eigenstates of the vibrational Hamiltonian.

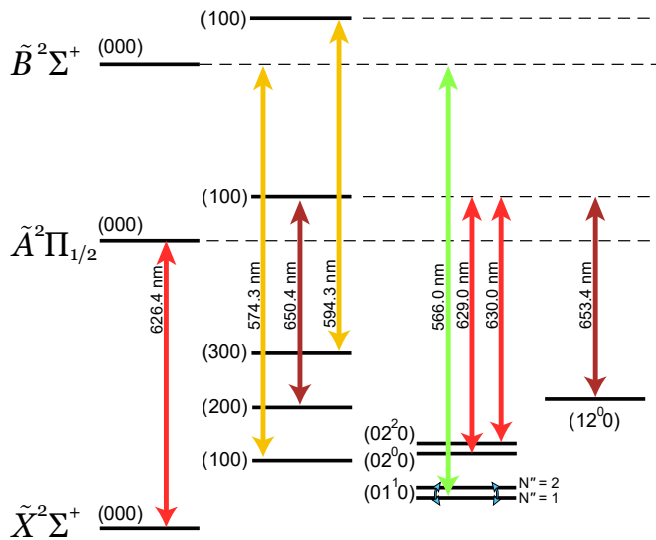


Figure 5. Photon cycling scheme and vibrational structure of CaOH to achieve the scattering of $\sim 10^4$ photons. All arrows represent transitions coupled by laser light. The $N'' = 1$ and $N'' = 2$ rotational components of the $\tilde{X}^2\Sigma^+(01^0)$ state may either be coupled by 40 GHz microwave radiation or directly addressed by frequency modulation of the laser radiation.

$\tilde{X}(300)$ is predicted to occur at the $\sim 10^{-6}$ level based on harmonic calculations, it is likely that anharmonicity in the potential energy function will significantly enhance loss to this state. Preliminary experimental measurements indeed suggest that the VBR to $\tilde{X}(300)$ may be as large as $\sim 1 \times 10^{-4}$. Finally, decay to the O–H stretching mode may be significant at this level, as experimental uncertainty in the O–H bond length makes calculations for this state unreliable.

Taken together, it is expected that 2–3 additional repump-

ing lasers, in addition to remixing of the $\tilde{X}(01^0)(N'' = 1, 2)$ levels via microwave radiation or laser frequency modulation, will be necessary to scatter $> 10^4$ photons in CaOH. One proposed cycling scheme is illustrated in Fig. 5. This should be sufficient to enable radiative slowing and magneto-optical trapping of CaOH molecules.

IV. CONCLUSION

This work establishes a vibrational repumping scheme enabling deep laser cooling and control of CaOH despite its complex internal structure. Our experimental measurements validate calculations used to estimate higher-order decay pathways. Using these predictions, we propose a laser cooling scheme (shown in Fig. 5) capable of scattering $\sim 10^4$ photons, which will enable experimental efforts to implement radiative slowing, 3D magneto-optical trapping, and ultimately, deep laser cooling into the ultracold regime. The spectroscopy presented in Appendix C establishes a clear path towards the experimental implementation of this laser cooling scheme. While the measurements presented here are unique to CaOH, the experimental methods and calculations outline a general framework that could be used to predict and confirm VBRs in other molecular candidates for direct laser cooling. The insights gained here for CaOH can be generalized to support recent proposals extending laser cooling to symmetric and asymmetric top molecules [20, 24, 25] and even molecules with multiple cycling centers [54–57].

ACKNOWLEDGMENTS

We would like to thank L. Anderegg and Z. Lasner for insightful discussions. This work was supported by the NSF, AFOSR, and ARO. N.B.V. acknowledges funding from the NDSEG fellowship, and B.L.A. from the NSF GRFP.

-
- [1] S. Chu, *Rev. Mod. Phys.* **70**, 685 (1998).
 - [2] W. D. Phillips, *Rev. Mod. Phys.* **70**, 721 (1998).
 - [3] M. D. Swallows, M. Bishof, Y. Lin, S. Blatt, M. J. Martin, A. M. Rey, and J. Ye, *Science* **331**, 1043 (2011).
 - [4] I. Bloch, J. Dalibard, and W. Zwerger, *Rev. Mod. Phys.* **80**, 885 (2008).
 - [5] M. Endres, H. Bernien, A. Keesling, H. Levine, E. R. Anschuetz, A. Krajenbrink, C. Senko, V. Vuletic, M. Greiner, and M. D. Lukin, *Science* **354**, 1024 (2016).
 - [6] H. Bernien, S. Schwartz, A. Keesling, H. Levine, A. Omran, H. Pichler, S. Choi, A. S. Zibrov, M. Endres, M. Greiner, *et al.*, *Nature* **551**, 579 (2017).
 - [7] L. Anderegg, L. W. Cheuk, Y. Bao, S. Burchesky, W. Ketterle, K.-K. Ni, and J. M. Doyle, *Science* **365**, 1156 (2019).
 - [8] M. L. Wall, K. Maeda, and L. D. Carr, *Ann. Phys. (Berlin)* **525**, 845 (2013).
 - [9] M. Wall, K. Maeda, and L. D. Carr, *New J. Phys.* **17**, 025001 (2015).
 - [10] P. Yu, L. W. Cheuk, I. Kozyryev, and J. M. Doyle, *New J. Phys.* **21**, 093049 (2019).
 - [11] L. D. Augustovičová and J. L. Bohn, *New J. Phys.* **21**, 103022 (2019).
 - [12] J. L. Bohn, A. M. Rey, and J. Ye, *Science* **357**, 1002 (2017).
 - [13] I. Kozyryev and N. R. Hutzler, *Phys. Rev. Lett.* **119**, 133002 (2017).
 - [14] I. Kozyryev, Z. Lasner, and J. M. Doyle, *arXiv:1805.08185* (2018).
 - [15] E. B. Norrgard, D. S. Barker, S. Eckel, J. A. Fedchak, N. N. Klimov, and J. Scherschligt, *Communications Physics* **2**, 77 (2019).
 - [16] I. Kozyryev, L. Baum, K. Matsuda, B. L. Augenbraun, L. Anderegg, A. P. Sedlack, and J. M. Doyle, *Phys. Rev. Lett.* **118**, 173201 (2017).
 - [17] I. Kozyryev, L. Baum, L. Aldridge, P. Yu, E. E. Eyler, and J. M. Doyle, *Phys. Rev. Lett.* **120**, 063205 (2018).
 - [18] B. L. Augenbraun, Z. D. Lasner, A. Frenett, H. Sawaoka, C. Miller, T. C. Steimle, and J. M. Doyle, *New J. Phys.* **22**,

- 022003 (2020).
- [19] L. Baum, N. B. Vilas, C. Hallas, B. L. Augenbraun, S. Raval, D. Mitra, and J. M. Doyle, *Phys. Rev. Lett.* **124**, 133201 (2020).
- [20] D. Mitra, N. B. Vilas, C. Hallas, L. Anderegg, B. L. Augenbraun, L. Baum, C. Miller, S. Raval, and J. M. Doyle, [arXiv:2004.02848](https://arxiv.org/abs/2004.02848) (2020).
- [21] I. Kozyryev, T. C. Steimle, P. Yu, D.-T. Nguyen, and J. M. Doyle, *New J. Phys.* **21**, 052002 (2019).
- [22] E. T. Mengesha, A. T. Le, T. C. Steimle, L. Cheng, C. Zhang, B. L. Augenbraun, Z. Lasner, and J. Doyle, *J. Phys. Chem. A* **124**, 3135 (2020).
- [23] D.-T. Nguyen, T. C. Steimle, I. Kozyryev, M. Huang, and A. B. McCoy, *J. Mol. Spectrosc.* **347**, 7 (2018).
- [24] I. Kozyryev, L. Baum, K. Matsuda, and J. M. Doyle, *ChemPhysChem* **17**, 3641 (2016).
- [25] B. L. Augenbraun, J. M. Doyle, T. Zelevinsky, and I. Kozyryev, [arXiv:2001.11020](https://arxiv.org/abs/2001.11020) (2020).
- [26] G. Herzberg, *Molecular spectra and molecular structure. Vol. 3: Electronic spectra and electronic structure of polyatomic molecules* (New York: Van Nostrand, Reinhold, 1966).
- [27] M. Di Rosa, *Eur. Phys. J. D* **31**, 395 (2004).
- [28] C. Scurlock, D. Fletcher, and T. Steimle, *J. Mol. Spectrosc.* **159**, 350 (1993).
- [29] N. R. Hutzler, H.-I. Lu, and J. M. Doyle, *Chem. Rev.* **112**, 4803 (2012).
- [30] E. Norrgard, D. McCarron, M. Steinecker, M. Tarbutt, and D. DeMille, *Phys. Rev. Lett.* **116**, 063004 (2016).
- [31] M. Tarbutt, B. Sauer, J. Hudson, and E. Hinds, *New J. Phys.* **15**, 053034 (2013).
- [32] P. F. Bernath, *Spectra of Atoms and Molecules* (New York: Oxford University Press, 2005).
- [33] L. T. Earls, *Phys. Rev.* **48**, 423 (1935).
- [34] E. B. Wilson, J. C. Decius, and P. C. Cross, *Molecular Vibrations: The Theory of Infrared and Raman Vibrational Spectra* (New York: Dover Publications, 1955).
- [35] T. Sharp and H. Rosenstock, *J. Chem. Phys.* **41**, 3453 (1964).
- [36] J. Weber and G. Hohlneicher, *Mol. Phys.* **101**, 2125 (2003).
- [37] C. Brazier and P. Bernath, *J. Mol. Spectrosc.* **114**, 163 (1985).
- [38] S. Kinsey-Nielsen, C. R. Brazier, and P. F. Bernath, *J. Chem. Phys.* **84**, 698 (1986).
- [39] J. A. Coxon, M. Li, and P. I. Presunka, *J. Mol. Spectrosc.* **164**, 118 (1994).
- [40] J. Aarts, *Mol. Phys.* **35**, 1785 (1978).
- [41] J. M. Brown and F. Jorgensen, in *Advances in Chemical Physics, Volume LII*, edited by I. Prigogine and S. A. Rice (Wiley & Sons Ltd., 1983) pp. 117–180.
- [42] P. Jensen, G. Osmann, and P. R. Bunker, in *Computational Molecular Spectroscopy*, edited by P. Jensen and P. R. Bunker (Wiley & Sons Ltd., 2000) Chap. 15, pp. 485–515.
- [43] J. M. Brown, in *Computational Molecular Spectroscopy*, edited by P. Jensen and P. R. Bunker (Wiley & Sons Ltd., 2000) Chap. 16, pp. 517–537.
- [44] J. M. Brown, *Mol. Phys.* **101**, 3419 (2003).
- [45] E. Hirota, *High-resolution spectroscopy of transient molecules*, Vol. 40 (Springer Science & Business Media, 2012).
- [46] M. Li and J. A. Coxon, *J. Mol. Spectrosc.* **183**, 250 (1997).
- [47] G. Fischer, *Vibronic Coupling: The Interaction between the Electronic and Nuclear Motions* (Academic Press, 1984).
- [48] M. Li and J. A. Coxon, *J. Chem. Phys.* **102**, 2663 (1995).
- [49] M. Li and J. A. Coxon, *J. Chem. Phys.* **97**, 8961 (1992).
- [50] M. Li, *High-resolution laser spectroscopy of the $\tilde{A}^2\Pi - \tilde{X}^2\Sigma^+$ system of calcium hydroxyl and calcium hydroxyl-d radicals*, *Ph.D. thesis*, Dalhousie University (1995).
- [51] M. Li and J. A. Coxon, *J. Chem. Phys.* **104**, 4961 (1996).
- [52] E. Fermi, *Zeitschrift für Physik* **71**, 250 (1931).
- [53] J. T. Hougen, *J. Chem. Phys.* **37**, 403 (1962).
- [54] M. J. O'Rourke and N. R. Hutzler, *Phys. Rev. A* **100**, 022502 (2019).
- [55] B. Ostojic, P. Jensen, P. Schwerdtfeger, and P. Bunker, *J. Phys. Chem. A* **117**, 9370 (2013).
- [56] M. V. Ivanov, S. Gulania, and A. I. Krylov, *J. Phys. Chem. Lett.* **11**, 1297 (2020).
- [57] J. Klos and S. Kotochigova, *Phys. Rev. Research* **2**, 013384 (2020).
- [58] M. Dick, P. Sheridan, J.-G. Wang, S. Yu, and P. Bernath, *J. Mol. Spectrosc.* **240**, 238 (2006).
- [59] C. M. Taylor, R. K. Chaudhuri, and K. F. Freed, *J. Chem. Phys.* **122**, 044317 (2005).
- [60] J. A. Coxon, M. Li, and P. I. Presunka, *Mol. Phys.* **76**, 1463 (1992).
- [61] R. Pereira and D. H. Levy, *J. Chem. Phys.* **105**, 9733 (1996).
- [62] L. Anderegg, *Ultracold molecules in optical arrays: from laser cooling to molecular collisions*, *Ph.D. thesis*, Harvard University (2019).
- [63] E. Salumbides, V. Maslinskas, I. Dildar, A. Wolf, E.-J. Van Duijn, K. Eikema, and W. Ubachs, *Phys. Rev. A* **83**, 012502 (2011).

Appendix A: FCF Calculations

The vibrational overlap integrals of Eq. 6 are calculated by assuming harmonic oscillator wavefunctions. The calculation employs the Wilson GF normal coordinate analysis and the Sharp-Rosenstock method, as described in detail elsewhere [21, 34–36].

Briefly, we begin by constructing the Wilson force and kinetic energy-related matrices \mathbf{F} and \mathbf{G} , which are related to the vibrational potential energy V and kinetic energy K by

$$2V = (\vec{S})^T \mathbf{F} \vec{S}, \quad 2K = (\dot{\vec{S}})^T \mathbf{G}^{-1} \dot{\vec{S}} \quad (\text{A1})$$

where \vec{S} is a vector of $3N - 5$ internal molecular coordinates and $[\dots]^T$ denotes the vector transpose. For CaOH, we define the internal coordinates so that $S_1 = \Delta r_{31}$, $S_2 = \Delta r_{32}$ and $S_3 = (r_{31} r_{32})^{1/2} \Delta\phi$, where r_{31} and r_{32} are the equilibrium Ca–O and O–H bond lengths, respectively, Δr_{31} and Δr_{32} give the change in bond length, and $\Delta\phi$ is the change in the bending angle. From geometrical arguments the \mathbf{G} matrix can be expressed as [34]

$$\mathbf{G} = \begin{pmatrix} \mu_1 + \mu_3 & -\mu_3 & 0 \\ -\mu_3 & \mu_2 + \mu_3 & 0 \\ 0 & 0 & G_{33} \end{pmatrix}, \quad G_{33} = \mu_1 \frac{r_{32}}{r_{31}} + \mu_2 \frac{r_{31}}{r_{32}} + \mu_3 \frac{(r_{31} + r_{32})^2}{r_{31} r_{32}} \quad (\text{A2})$$

where $\mu_1 = 1/m_{\text{Ca}}$, $\mu_2 = 1/m_{\text{H}}$, $\mu_3 = 1/m_{\text{O}}$.

The \mathbf{F} matrix consists of second derivatives of the potential energy surface with respect to the internal coordinates. Because there is at most only very weak coupling between the

stretching and bending vibrations, we write \mathbf{F} as

$$\mathbf{F} = \begin{pmatrix} F_{11} & F_{12} & 0 \\ F_{21} & F_{22} & 0 \\ 0 & 0 & F_{33} \end{pmatrix} \quad (\text{A3})$$

Diagonalizing the matrix product \mathbf{GF} is equivalent to solving the secular equation, and its eigenvalues and eigenvectors are the frequencies and coordinates of the normal modes of vibration. In particular, properly-normalized eigenvectors of \mathbf{GF} form the columns of the \mathbf{L} matrix, which transforms normal coordinates \tilde{Q} into internal coordinates $\tilde{S} = \mathbf{L}\tilde{Q}$.

For the $\tilde{A} \rightarrow \tilde{X}$ transition, we use measured vibrational frequencies and bond lengths from Ref. [51] to solve for the force constants F_{ij} . This calculation makes use of equations given in Refs. [48, 51]. For the $\tilde{B} \rightarrow \tilde{X}$ transition we use the measured bond lengths from Ref. [58], in conjunction with vibrational frequency calculations from Ref. [59]. There is insufficient data on the \tilde{B} state to extract the off-diagonal force constants (these require data from CaOD as well), so we make the approximation that $F_{21} = F_{12} = 0$ for the \tilde{B} state. We find that this has little impact on the final result.

After solving for the normal modes using the \mathbf{GF} matrix approach, harmonic overlap integrals may be factored as

$$\langle v'' | v' \rangle = \prod_i \int \Psi_{v_i''}^* \Psi_{v_i'} dQ_i, \quad (\text{A4})$$

where Ψ_{v_i} is a harmonic oscillator eigenfunction and Q_i is a normal coordinate. Eq. A4 may be evaluated by transforming the normal coordinates \tilde{Q}'' of the final state to those of the initial state \tilde{Q}' via a Duschinsky rotation,

$$\tilde{Q}' = \mathbf{J}\tilde{Q}'' + \tilde{K}. \quad (\text{A5})$$

The method employed here, due to Sharp and Rosenstock, relates \mathbf{J} and \tilde{K} to the transformation matrices \mathbf{L}'' , \mathbf{L}' of the ground and excited states, as well as their equilibrium geometries. The solution makes use of generating functions, and the results may be calculated using standard computational tools [35, 36].

In the case where the vibrational eigenstates are mixed by perturbations to the potential energy surface (as in the Renner-Teller and Fermi resonance interactions discussed above), FCFs may still be computed using the harmonic calculations described here. For example, if the ground and excited state vibrational wavefunctions are given by

$$|v'\rangle = a|\bar{v}'_a\rangle + b|\bar{v}'_b\rangle, \quad |v''\rangle = c|\bar{v}''_a\rangle + d|\bar{v}''_b\rangle,$$

where the horizontal bar denotes a harmonic oscillator eigenstate, the FCF is

$$q_{v'-v''} = |\langle v'' | v' \rangle|^2 \\ = \left| a^* c \langle \bar{v}''_a | \bar{v}'_a \rangle + a^* d \langle \bar{v}''_a | \bar{v}'_b \rangle + \dots \right|^2$$

where each term on the right-hand side is a harmonic overlap integral (Eq. A4) and can be computed by the means described above.

Appendix B: Fermi Resonance Matrix Elements

The nonzero matrix elements of the Fermi resonance operator $V_F = k_{122}Q_1Q_2^2$ for a non-degenerate vibronic state are [53]

$$\langle v_1 + 1, v_2, v_3; l | V_F | v_1, v_2 + 2, v_3; l \rangle \\ = W [(v_1 + 1)(v_2 + 2 - l)(v_2 + 2 + l)]^{1/2} \quad (\text{B1a})$$

$$\langle v_1 + 1, v_2, v_3; l | V_F | v_1, v_2, v_3; l \rangle \\ = 2W (v_1 + 1)^{1/2} (v_2 + 1) \quad (\text{B1b})$$

where

$$W = \frac{k_{122}}{2\sqrt{2}} \left(\frac{\hbar}{\omega_2} \right) \left(\frac{\hbar}{\omega_1} \right)^{1/2} \quad (\text{B2})$$

is the Fermi resonance parameter and depends on only the force constant k_{122} , the Ca–O stretching frequency ω_1 , and the Ca–O–H bending frequency ω_2 .³ Because the second matrix element (Eq. B1b) connects states separated by a relatively large energy, its effects are neglected in this work. We note, however, that matrix elements of this sort generically arise from other anharmonic terms in the potential energy function as well. These couplings may contribute to higher-order decay channels, though a full analysis of such effects is beyond the scope of this work.

While the Fermi resonance parameter W has not been measured for the $\tilde{X}^2\Sigma^+$ state of CaOH, it has been fit in the $\tilde{A}^2\Pi$ state from an analysis of the (100) ~ (020) Fermi dyad [51]. Assuming that k_{122} is unchanged between the \tilde{X} and \tilde{A} states, and using measured vibrational frequencies $\omega_{1,2}$ [51], we estimate a Fermi resonance parameter $|W_X| \approx 10.7 \text{ cm}^{-1}$ in the $\tilde{X}^2\Sigma^+$ state by scaling the \tilde{A} state measurement by the appropriate factors in Eq. B2. This is in good agreement with a separate estimate $|W_X| \approx 11.1 \text{ cm}^{-1}$ obtained directly from spectroscopy of the $\tilde{X}(02^0_0) - \tilde{X}(02^2_0)$ and $\tilde{X}(12^0_0) - \tilde{X}(12^2_0)$ bending mode pairs. While the sign of W was not determined experimentally in Ref. [51], by relating W to other measured constants it was deduced in that work that $W < 0$.

Appendix C: Spectroscopy of Combination Bands

While high-resolution spectroscopy exists for the (300), (400), and (01¹0) vibrational manifolds of the $\tilde{X}^2\Sigma^+$ state [48, 60], there is no such data for the (120) manifold required to achieve a MOT of CaOH.⁴ Therefore, high-resolution spectroscopy of the $\tilde{X}(12^0_0)$ and $\tilde{X}(12^2_0)$ repumping transitions was performed here.

Population of the $\tilde{X}(12^0_0)$ ($\tilde{X}(12^2_0)$) state was enhanced via off-diagonal vibronic decay after exciting molecules on

³ Note that here the ω_i have units of angular frequency, while equations elsewhere in the literature typically have them in cm^{-1} .

⁴ This manifold was, however, observed at low resolution in Ref. [61].

$\tilde{A}(100) - \tilde{X}(12^0_0)$				
J	P_{11}	${}^P Q_{12}$	Q_{11}	${}^Q R_{12}$
1/2		458.789108		458.817435
3/2	458.789055		458.817383	
$\tilde{A}(02^0_0) - \tilde{X}(12^0_0)$				
J	P_{11}	${}^P Q_{12}$		
1/2		460.878315		
3/2	460.878262			
$\tilde{A}(100) - \tilde{X}(12^2_0)$				
J	${}^O P_{12}$		${}^P Q_{12}$	
3/2	458.179688		458.208017	
$\tilde{A}(02^0_0) - \tilde{X}(12^2_0)$				
J	${}^O P_{12}$			
3/2	460.068935			

Table II. Transitions observed during this work. Reported in units of THz. The uncertainty in absolute frequency (~ 150 MHz) is estimated by comparing several measured transitions to accepted literature values, any correction would apply uniformly. The error in relative frequency (~ 10 MHz) is limited by the fit to the Doppler broadened lineshape.

the $\tilde{X}(000) \rightarrow \tilde{A}(02^0_0)$ ($\tilde{X}(000) \rightarrow \tilde{A}(02^2_0)$) P_1 ($N'' = 1$) and ${}^P Q_{12}$ ($N'' = 1$) transitions.⁵ This ensured that only the ($N'' = 1, J'' = 1/2, 3/2$) rotational states relevant to laser cooling would be populated. A cw dye laser was then scanned over the repumping transition of interest. Several rovibronic transitions were observed; the absolute frequency of these transitions is reported in Table II. The relative frequency of the excitation laser was referenced to a High Finesse WS7 wavemeter. Empirically, the relative accuracy of the wavemeter has been verified to < 1 MHz when continuously calibrated with an atomic reference [62]. The absolute frequency was obtained by referencing the observed calcium $4^1S_0 \rightarrow 4^3P_1$ intercombination line to the accepted literature value [63]. The frequency offset (relative frequency – absolute frequency) is assumed to be constant, and this constant correction is applied to the transitions reported in Table II. Several other known atomic and molecular transitions have been observed using this frequency reference, and the standard deviation of the frequency offsets from these measurements is ~ 150 MHz. Rotational assignments were verified by selectively populating only specific rotational ground states as described above, and by confirming that the observed rotational spacings and spin-orbit splittings were consistent with the assignments.

⁵ For notational clarity, we label the \tilde{A} state vibrational levels by their

dominant character. Specifically, the correspondence is $\tilde{A}(02^0_0) \rightarrow \tilde{A}(020)_{\mu^2\Pi_{1/2}}$ and $\tilde{A}(02^2_0) \rightarrow \tilde{A}(020)_{\kappa^2\Pi_{1/2}}$ in the notation of Ref. [51].